

Evidence of Homogeneous Microstructures in Ti6Al4V Alloy During Shear Deformation



R. VINJAMURI, B.D. BISHOYI, R.K. SABAT, M. KUMAR, and S.K. SAHOO

Free-end torsion tests were conducted for Ti6Al4V (Ti64) alloy at temperatures of 298 K, 673 K, and 873 K for different strains ranging from 0.22 to 0.99. The microstructure and texture evolution as a function of torsional deformation have been investigated in the present study. A near-equiaxed homogeneous microstructure was observed after deformation at all temperatures. However, the grains were observed to be aligned along the direction of shear stress at larger deformation strains. Dynamically recrystallized (DRX) grains were observed in the samples at higher deformation temperatures, and these were found to be significant at 873 K for strains > 0.66. Dynamic transformation of $\alpha \rightarrow \beta$ was also observed during deformation at a temperature of 873 K. The initial fiber texture got rotated toward the ideal B fiber orientation, and reached at the ideal C2 fiber orientation after deformation for a maximum strain of 0.99. The deformation texture was further simulated through the Visco plastic self-consistent (VPSC) method, and it was found that the basal slip was the dominant deformation mode followed by prismatic and both pyramidal $\langle c+a \rangle$ I and II slip systems. The flow stress decreased with increase in the temperature of deformation, and a significant flow softening was observed during deformation at 873 K.

<https://doi.org/10.1007/s11661-022-06657-7>

© The Minerals, Metals & Materials Society and ASM International 2022

I. INTRODUCTION

Ti6Al4V (Ti64) alloy is an essential alloy for applications in the aerospace, chemical, and marine sectors due to its high strength-to-weight ratio, superior corrosion resistance, and outstanding fatigue and fracture properties.^[1–3] These properties of Ti64 can be improved by controlling the microstructure and texture evolution during different plastic deformation processes.^[4] Ti64 alloys with fine and homogeneous equiaxed microstructure were mainly used as structural components in aviation industries due to their enhanced properties, such as higher ductility, and better creep and fatigue resistances.^[3,5] Also, the equiaxed grains with homogeneous microstructures can promote the super plastic deformation at lower temperatures.^[3,6] Hence, control over microstructural homogeneity can have a greater significance to optimize the required properties of Ti64 alloy. Shear deformation plays a major role in producing equiaxed grains by fragmentation of lamellar microstructures, as reported by many

researchers.^[6–9] Deformation through torsion has been successfully employed to materials for achieving large shear strains without rupture or strain localization.^[10,11]

The texture and microstructure evolution during torsional deformation are rather well known for cubic materials than HCP (hexagonal close packed) materials.^[12–15] Initially, Sanchez *et al.*^[16] have investigated the texture developments during torsion experiments on Zirconium alloys. Later on, many authors carried out their research on magnesium and its alloys^[17–21] and pure titanium.^[22–25] Beausir *et al.*^[26] have identified five types of ideal fiber texture components (B, P, Y, and C1–C2) for HCP metals when they are subjected to simple shear deformation. Gurao *et al.* performed free-end torsion tests on pure titanium in the strain rate regime of 0.001 to 1 s⁻¹ and observed the formation of C1 fiber texture in deformed samples. Also, they noticed that the pyramidal $\langle c+a \rangle$ slip system was the main deformation mode, which is responsible for the deformation texture in absence of twinning. Recently, Bishoyi *et al.*^[40] have studied the effect of shear deformation on pure titanium by conducting free-end torsion tests. They found unstable C1 and C2 fiber textures in the samples during deformation along with ideal B fiber formation at high-temperature (873 K) deformation. Guo *et al.*^[27] have studied the dynamic transformation behavior of the Ti64 alloy by conducting torsion tests in the temperature range of 880–1000 °C. They observed the transformation of alpha phase to beta phase increases

R. VINJAMURI, B. D. BISHOYI, M. KUMAR, and S. K. SAHOO are with the Department of Metallurgical & Materials Engineering, NIT Rourkela, 769008, India. R. K. SABAT is with the School of Minerals, Metallurgical and Materials Engineering, IIT Bhubaneswar, 752050, India Contact e-mail: santoshsahoo@nitrkl.ac.in.

Manuscript submitted December 25, 2021; accepted March 9, 2022.

Article published online April 1, 2022

with strain and temperature in the two phase region. Also, the flow softening behavior was noticed along with dynamic transformation during isothermal multi-pass torsion tests at a temperature of 940 °C.^[28] From the above literature, it can be observed that the microstructure and texture evolution during torsional deformation of Ti64 alloy are rarely explored. The present investigation makes an effort to understand the deformation behavior and mechanism of microstructure and texture evolution during torsional deformation of Ti64 alloy. The free-end torsion tests were conducted on Ti64 alloy at three different temperatures: 298 K, 673 K, and 873 K for strain levels of 0.22, 0.44, 0.66, 0.88, and 0.99 respectively. The microstructure and texture evolution as a function of deformation strains and temperatures have been investigated in the present study. VPSC simulation was performed to understand the relative activities of slip systems during the deformation.

II. EXPERIMENTAL WORK

A. Sample Preparation

The Ti64 rods of diameter 15 mm were machined according to ASTM E143 as shown in Figure 1(a) for torsional deformation. The samples were subjected to free-end torsion tests in a Biss 100 Nm torsion system at a constant twist rate of 1 deg/s. The tests were carried out at three different temperatures of 298 K, 673 K, and 873 K for shear strains of 0.22, 0.44, 0.66, 0.88, and 0.99 respectively. The samples deformed at high temperatures were immediately quenched in water to stabilize the deformed microstructures. Samples were cut from the deformed specimens for subsequent characterization, which was carried out on the longitudinal surface parallel to the axial direction, near to the outer radius as shown in Figure 1(b). The sample surfaces were metallographically polished and electro-polished for microstructural and textural characterizations. Electro-polishing was carried out by using an electrolyte of methanol and perchloric acid (in the ratio of 80:20).

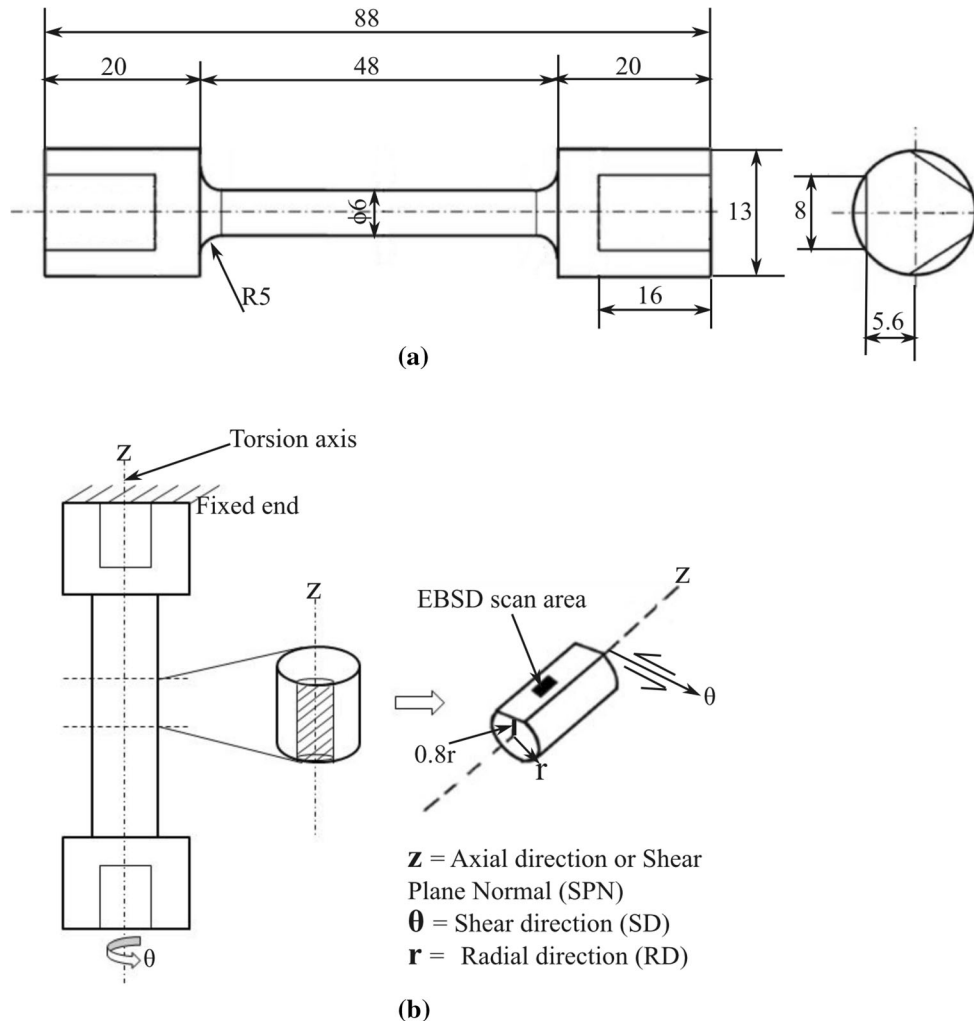


Fig. 1—Schematic diagram of specimen used in the present study: (a) Specimen used for torsion tests; (b) sample prepared for subsequent characterization. All dimensions marked in (a) are in mm.

B. Electron Back Scattered Diffraction (EBSD)

EBSD was carried out in an FEI Quanta 3D FEG scanning electron microscope for an approximate scanning area of $500\ \mu\text{m} \times 500\ \mu\text{m}$. A step size of $0.2\ \mu\text{m}$ with identical beam and video conditions was used. The EBSD scans were analyzed using TSL-OIM Version 6.2

software. In this analysis, grains were identified based on 15 deg misorientation criterion between each neighboring points. Misorientations inside the grains were estimated as grain orientation spread (GOS) and kernel average misorientation (KAM). GOS is defined as the misorientation between all the measurement points in a

Table I. Voce Hardening Parameters for Different Slip Systems Used in VPSC Simulation

Slip Systems	τ_0			τ_1			θ_0			θ_1		
	298 K	673 K	873 K	298 K	673 K	873 K	298 K	673 K	873 K	298 K	673 K	873 K
Basal	50	50	40	10	10	-5	15	15	-15	10	5	-6
Prismatic	120	130	70	10	10	-5	15	15	-15	10	5	-6
Pyramidal <a>	290	220	160	10	15	1	20	20	3	10	5	2
Pyramidal <c+a> I	320	200	130	10	15	1	20	20	3	10	5	2
Pyramidal <c+a> II	330	220	130	10	15	1	20	20	3	10	5	2

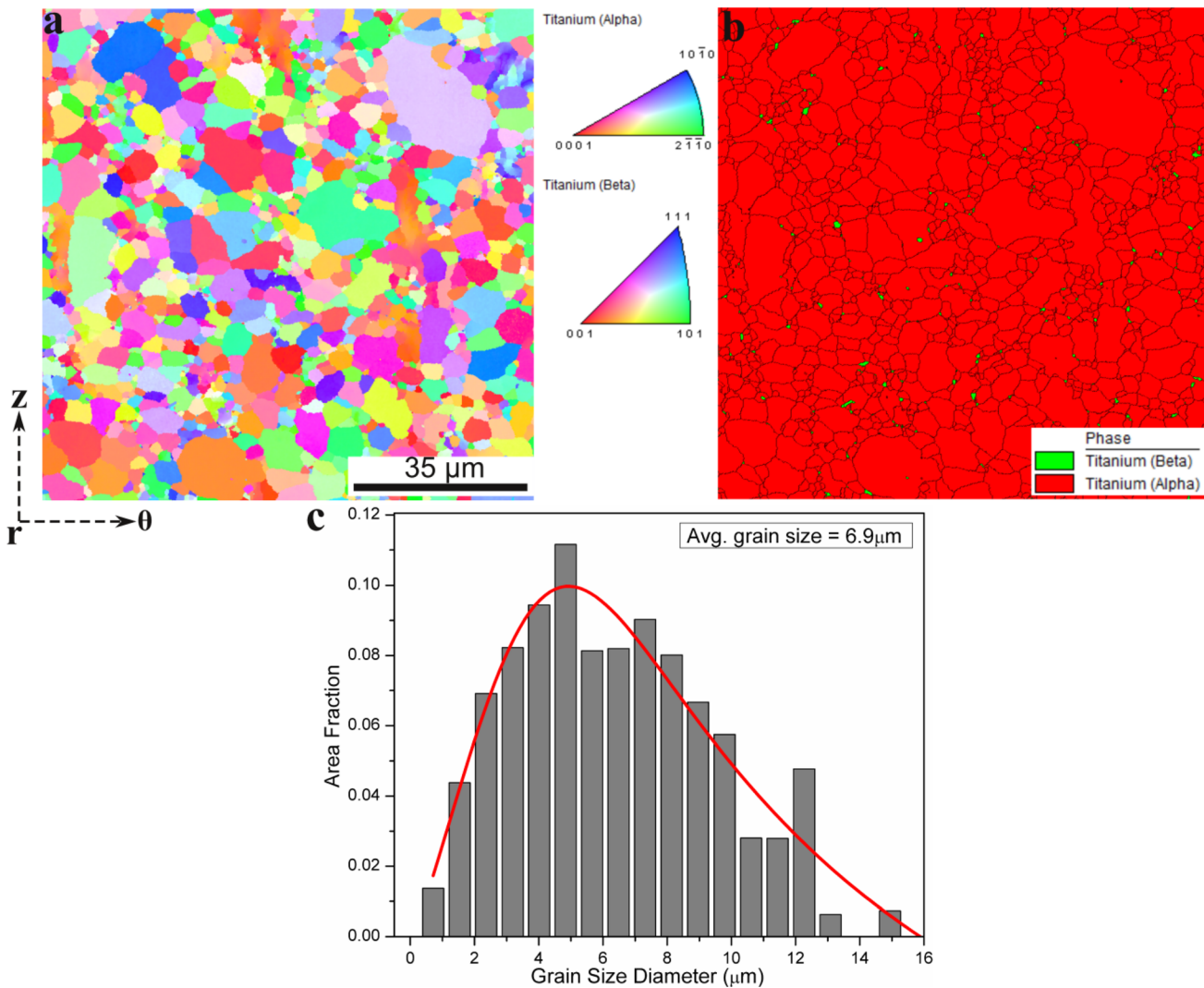


Fig. 2—Microstructure of the as-received Ti64 sample before subjected to torsion tests: (a) inverse pole figure (IPF) map; (b) phase map; (c) grain size distribution.

grain and the grain average orientation. KAM was measured by calculating the average misorientation of a kernel (center) point with its nearest neighbor points.

C. X-ray Diffraction (XRD)

A Bruker D8 advance system with a cobalt radiation source of 2 mm spot size was used for XRD measurements. Six poles, such as (0002), (10 $\bar{1}$ 0), (10 $\bar{1}$ 1), (10 $\bar{1}$ 2), (11 $\bar{2}$ 0), and (10 $\bar{1}$ 3) were measured for texture analysis. The texture results are represented using the free Matlab toolbox, MTEX.

III. VISCO PLASTIC SELF-CONSISTENT (VPSC) SIMULATION

The Version 7 of the Los Alamos VPSC code was used to predict the texture evolution and relative activities of various deformation modes during shear deformation.^[29] Bulk texture of the as-received sample obtained from an XRD measurement was taken as input for the simulation. No twinning was observed in the experimental results, and hence, it has not been considered. Dynamic recrystallization (DRX) was observed in the samples deformed at high temperatures for larger strains. However, this was also not considered in the

simulation. Deformation modes, such as prismatic slip {10 $\bar{1}$ 0} <11 $\bar{2}$ 0>, basal slip {0002} <11 $\bar{2}$ 0>, pyramidal <a> slip {10 $\bar{1}$ 1} <11 $\bar{2}$ 0>, pyramidal <c+a> I slip {10 $\bar{1}$ 1} <11 $\bar{2}$ 3>, and pyramidal <c+a> II {11 $\bar{2}$ 2} <11 $\bar{2}$ 3>, were considered. At high-temperature simulations, strain rate sensitivity m was taken as 0.2. The voce hardening parameters for different slip systems were considered from the works of Zafferer *et al.*,^[30] and the values are shown in Table I which were found after comparing with the stress-strain plots of the present study.

The velocity gradient (L) used for simple shear process is as follows:

$$L = \dot{\gamma} \begin{pmatrix} 0 & -1 & 0 \\ 0 & 0 & 0 \\ 0 & 0 & 0 \end{pmatrix} \quad [1]$$

IV. RESULTS

The microstructure of the initial as-received sample is shown in Figure 2. The initial sample had a wider distribution of grains, consisting of both fine and coarse grains, with an average grain size of $\sim 7 \mu\text{m}$. The grain size distributions of α grains are presented in Figure 2, as

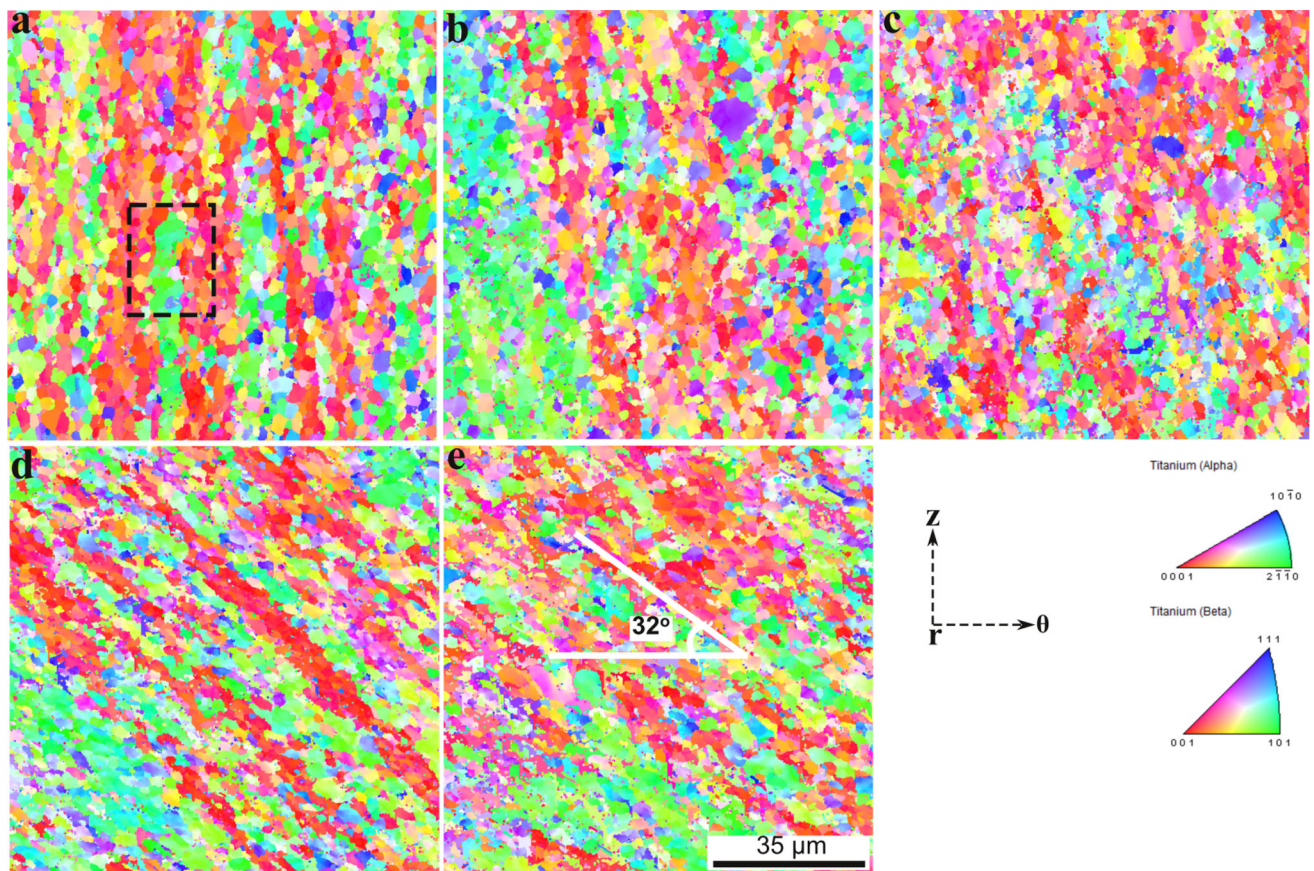


Fig. 3—IPF maps for the samples after deformation at a temperature of 298 K for different shear strains of: (a) 0.22; (b) 0.44; (c) 0.66; (d) 0.88; (e) 0.99. The region marked as black box in (a) is further presented in Fig. 15.

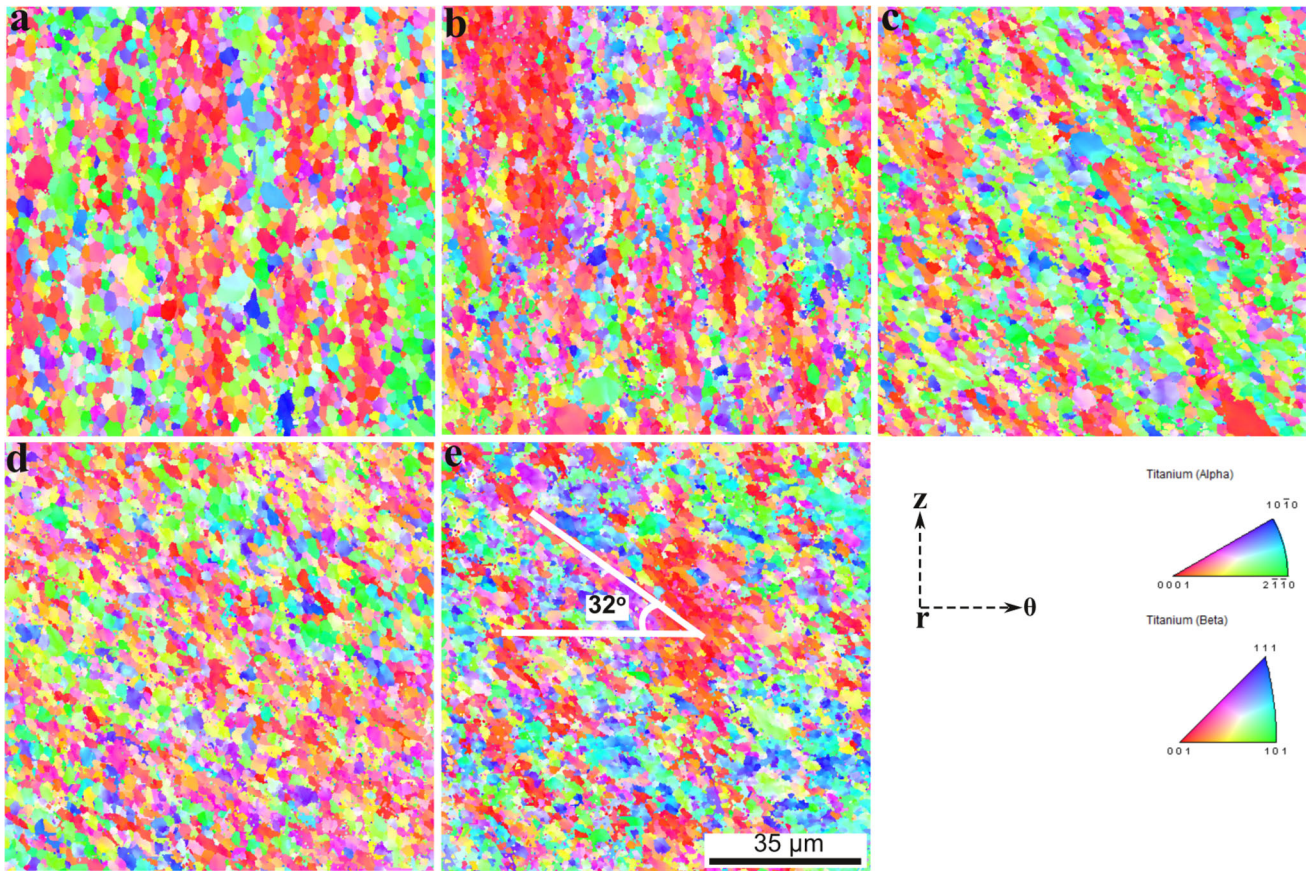


Fig. 4—IPF maps for the samples after deformation at a temperature of 673 K for different shear strains of: (a) 0.22; (b) 0.44; (c) 0.66; (d) 0.88; (e) 0.99.

the volume fraction of β grains was observed to be insignificant (< 1 pct) in the samples (Figure 2(b)). Figures 3, 4, 5 show the inverse pole figure (IPF) maps as a function of shear strains during deformations at various temperatures (298 K, 673 K, and 873 K). The samples showed a clear refinement of grains as a function of shear strain during deformation at all temperatures. However, the rate of grain refinement was observed to be maximum at an initial shear strain of 0.22. Further, a homogeneous distribution of grains can also be observed after deformation at all temperatures. The grains were observed to be aligned while increasing the shear strains in the samples during deformation. At the initial stages of deformation, most of the grains were near-equiaxed in nature and were seen to be aligned along the axial direction. With an increase in shear deformation, the alignment of the grains rotated toward the negative shear direction. At a shear strain of 0.99, the extent of rotation of the grains has been measured through the angle between the major axis of the grains and the shear direction. The rotation (R) of the grains was measured with respect to shear direction and was found to be around 32 deg for the samples deformed at temperatures of 298 K and 673 K, and around 40 deg for the samples deformed at 873 K. The measured angles at 298 K and 673 K are in accordance with the theoretical values, as reported by Canova *et al.*^[31]:

$$R = \frac{1}{2} \tan^{-1} \left(\frac{2}{\gamma} \right) \quad [2]$$

where R is the angle between the shear direction and the major axis of the grain, and γ is the shear strain produced during shear deformation. The value of R was found to be different for experimental and theoretical values of the sample deformed at a temperature of 873 K. It might be due to the dynamic softening behavior occurred at that deformation temperature. Further, no twinning was observed in the microstructures during deformation at all temperatures, which is generally observed in Ti64 alloy.^[32,33] The average grain size of the samples as a function of shear strains is shown in Figure 6(a). A decreasing trend in grain size of the samples as a function of deformation was observed at all temperatures of deformation. The misorientations inside the grains in terms of average GOS are shown in Figure 6(b). With an increase in shear deformation, the average GOS values were found to be increased at all temperatures of deformation. However, after deformation at a temperature of 873 K, the average GOS values got decreased after a shear strain of 0.44 (Figure 6(b)). The fraction of DRX grains at different temperatures of deformation is shown in Figure 6(c). The fraction of DRX grains was quantified as grains with an average

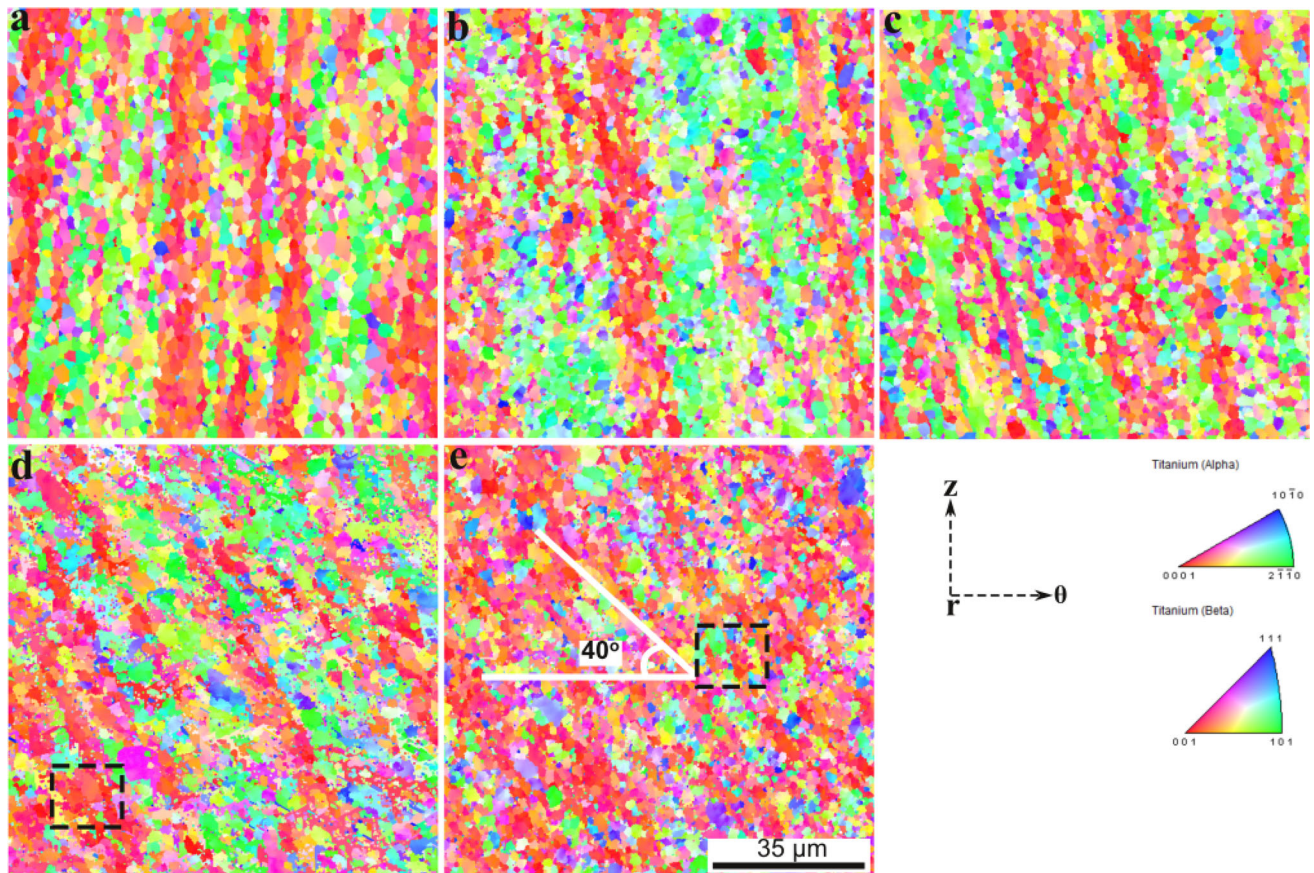


Fig. 5—IPF maps for the samples after deformation at a temperature of 873 K for different shear strains of: (a) 0.22; (b) 0.44; (c) 0.66; (d) 0.88; (e) 0.99. The regions marked as black boxes in (d, e) are further presented in Fig. 16.

GOS < 1 deg and an average grain size > 1 μm , which has been suggested by many researchers.^[24,34,35] It can be observed from Figure 6(c) that during deformation at 873 K, a significant increment of DRX grains was found at strains > 0.44.

Figure 7 shows the volume fraction of different grain boundaries, such as high-angle grain boundaries (HAGB), low-angle grain boundaries (LAGB), and very low-angle grain boundaries (VLAGB) at different temperatures of deformation. HAGB was characterized by the grain boundaries of misorientation 15 to 180 deg between the grains, and those of LAGB and VLAGB were 5 to 15 deg and 2 to 5 deg, respectively. An increment in VLAGB and a decrement in HAGB as a function of shear deformation were observed in the samples deformed at temperatures of 298 K and 673 K, although up to a shear deformation of 0.88. However, a reverse trend, *i.e.*, an increment in HAGB and a decrement in VLAGB, were noticed after a shear strain of 0.44 at 873 K. Figure 8 shows the KAM distribution maps of the samples before and after deformation. The average KAM distribution was observed to increase with the increase in shear strains at temperatures of 298 K and 673 K. However, deformation at 873 K also showed a decreased KAM distribution at a higher shear strain of 0.99. The volume fraction of β grains was observed to be increased during deformation at different

temperatures. This has been estimated in the TSL analysis software, and the results are presented in Figure 9. A noticeable increase in β phases was observed in the samples deformed at 873 K for shear strains > 0.66.

Figure 10 shows the texture, in terms of (0002) and (10 $\bar{1}$ 0) pole figures, and ODF at constant $\Phi = 90$ deg section, of the initial as-received sample. In both the pole figures and ODF, the ideal orientations observed^[26] during shear deformation of HCP metals/alloys are incorporated. The initial texture was represented by the plane consisting of axial direction (z) and shear direction (θ), which is normal to the radial direction (r). Five types of fibers are observed in HCP metals/alloys during shear deformation, *i.e.*, B fiber (0, 90, and 0 to 60), P fiber (0, 0 to 90 and 30), Y fiber (0, 30, and 0 to 60), C1 fiber (60, 90, and 0 to 60), and C2 fiber (120, 90, and 0 to 60), respectively.^[26] Figure 11 shows the bulk texture developments, in the form of (0002) and (10 $\bar{1}$ 0) pole figures, of the samples as a function of shear strain at three different temperatures. The initial samples had a fiber texture almost 90 deg to the ideal B fiber orientation (Figure 10(a)). With increasing shear deformation, this fiber rotated toward the ideal B fiber orientation (Figure 11). However, after the end of shear deformation, *i.e.*, at a shear strain of 0.99, this fiber was observed at the ideal C2 fiber orientation, which was at 60 deg

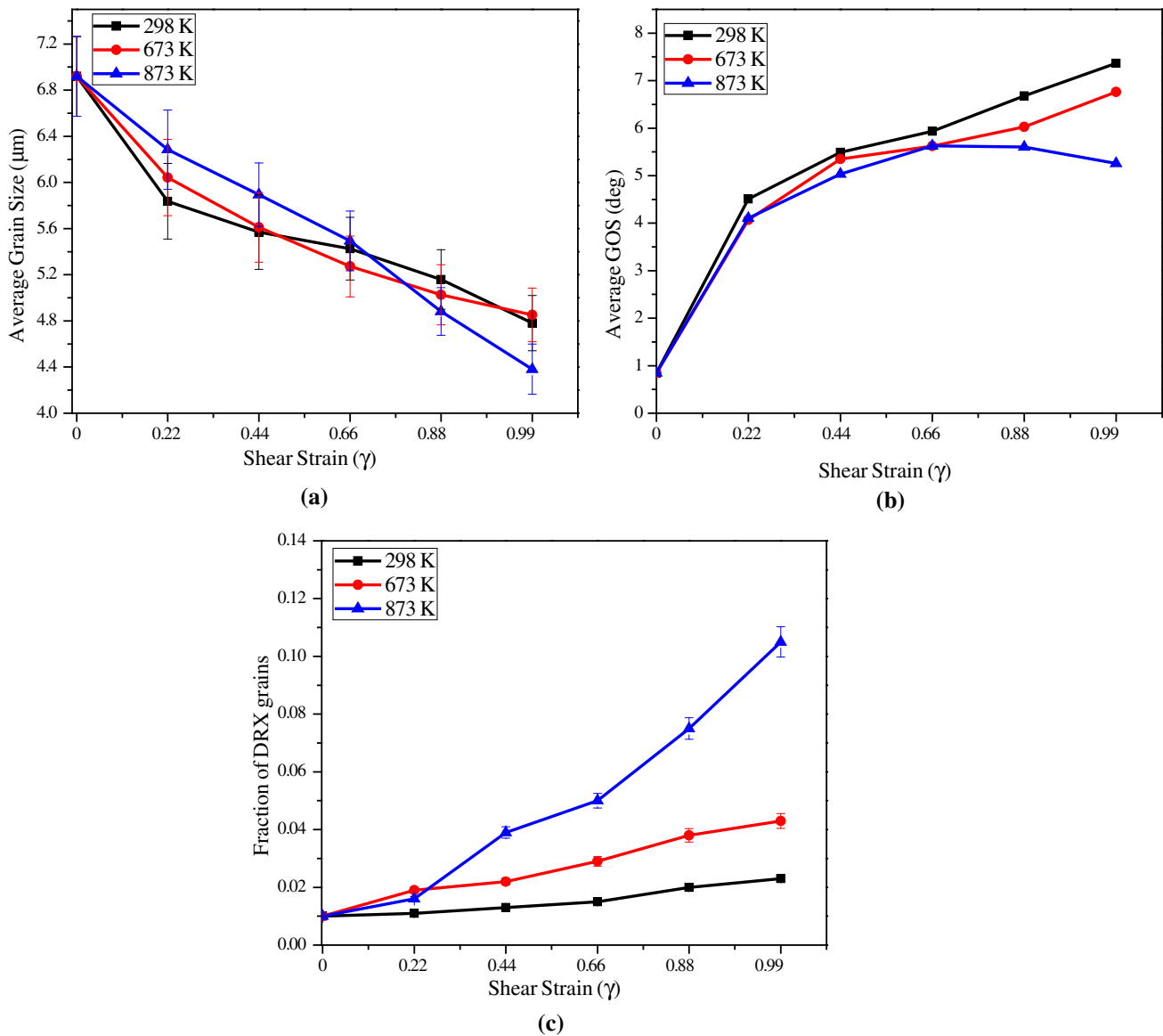


Fig. 6—(a) Average grain size, (b) average GOS, and (c) fraction of DRX of the samples as a function of shear strain after deformation at different temperatures.

from the ideal B fiber orientation (Figure 11). In Figure 11, the simulated textures obtained through VPSC simulation are also included, and these are discussed subsequently. As also observed from Figure 10(b), the initial undeformed sample had a fiber texture at $\varphi_1 = 90$ and 270 deg which was 90 deg away from the ideal B fiber orientation. Figure 12 shows the ODFs, at constant $\Phi = 90$ deg section, of the samples after deformation at different temperatures. It can be observed from Figure 12 that the initial fiber present at $\varphi_1 = 90$ deg position got shifted along higher φ_1 values and reached at the ideal C2 fiber orientation. Such movement in the fiber position was found to be identical at all three temperatures of deformation.

The shear stress–shear strain curves were determined from the torque–twist angle data using Nadai’s formulae,^[36] which are shown in Figure 13. A decrement in flow stress values with an increase in the temperature of deformation was observed. There was a noticeable flow softening occurred at a temperature of 873 K. The strain hardening rate $\theta = (\partial\tau/\partial\gamma)$ and its derivative $\theta^* = -(\partial\theta/\partial\tau)$ against shear stress values are presented in Figure 14. According to the Poliak-Jonas method,^[37] the onset of any dynamic restoration process can be known by the inflection points in $\theta^* = -(\partial\theta/\partial\tau)$ vs shear stress (τ) curves. The inflection points were observed at O, P, and Q for deformation temperatures of 298 K, 673 K, and 873 K, respectively (Figure 14). It was also observed

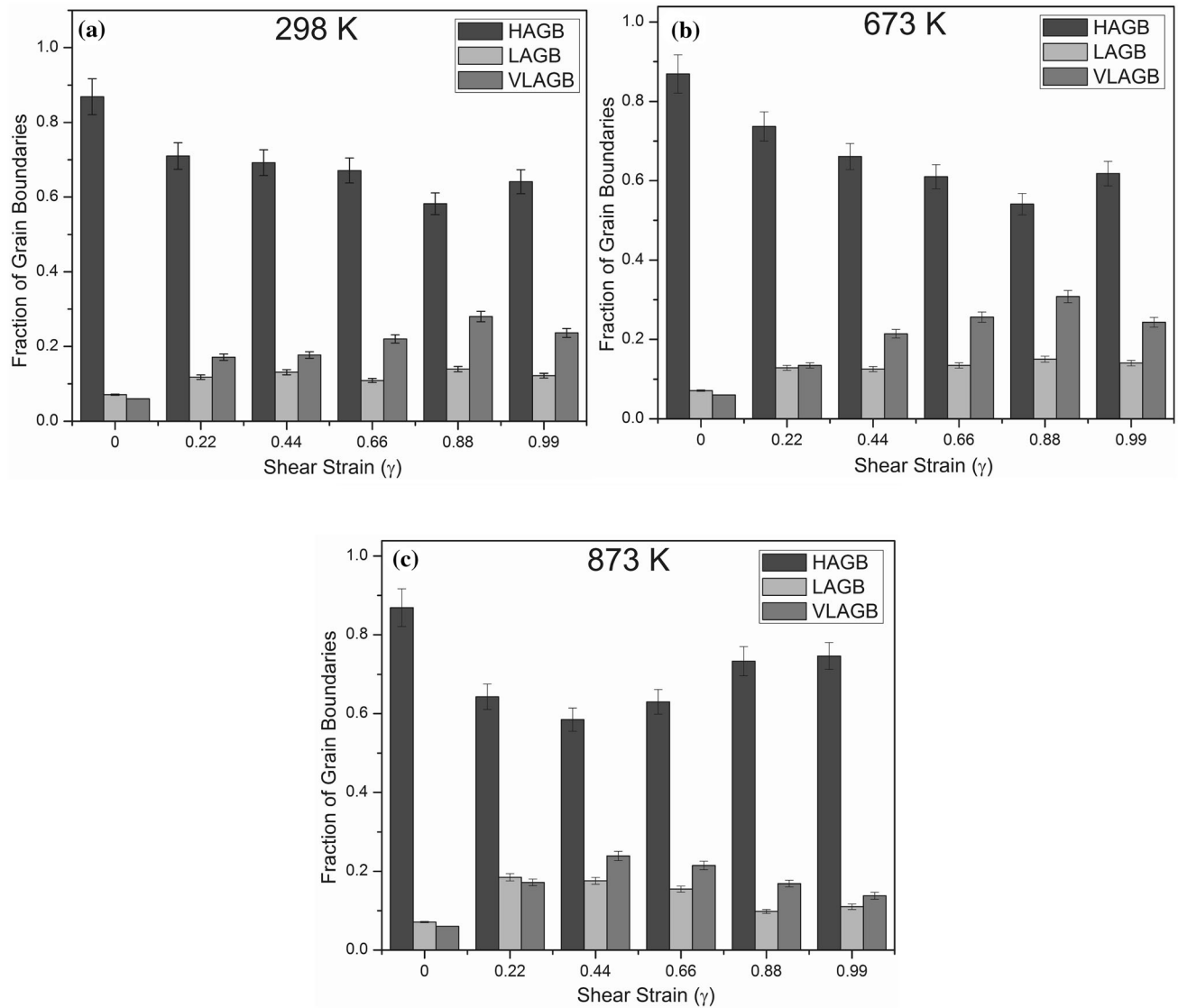


Fig. 7—Grain boundary fractions as a function of shear strain after deformation at different temperatures of: (a) 298 K; (b) 673 K; (c) 873 K.

from Figure 14 that the strain hardening rate was more at room temperature (298 K) deformation than those at high temperatures of deformation. Also, the hardening curves were observed to be shifted to lower stress values with increasing the temperature of deformation. Stage III and stage IV hardening with a decreased hardening rate were clearly observed at all three temperatures of deformation.

V. DISCUSSION

A. Microstructure Evolution

The observed microstructural evolution during shear deformation of Ti64 alloy can be distinguished from the previous studies^[6-9] as: (1) development of microstructural homogeneity, (2) grain refinement, (3) DRX grains, and (4) increment in β volume fraction.

The as-received Ti64 samples were comprised of a wider grain size distribution of both fine and coarse grains (Figure 2). After shear deformation, the samples show the refinement of the grains with a homogeneous grain size distribution (Figures 3, 4, 5). Such microstructural development in the samples under shear deformation can be understood through Figure 15. As suggested by Seshacharyulu *et al.*,^[38] shearing of grains favorably oriented along the applied shear stress will participate in the shearing process, which will rotate the neighboring grains into favorable orientation for facilitating the shearing process, and this will continue as a function of shear strain and may reach completion at larger strains. During shearing, dislocations get aligned along the line of shear, and the dislocations of the same sign are expected to nucleate an interface along the line of shear. However, the dislocations of opposite signs get annihilated during the deformation. The subgrain thus formed

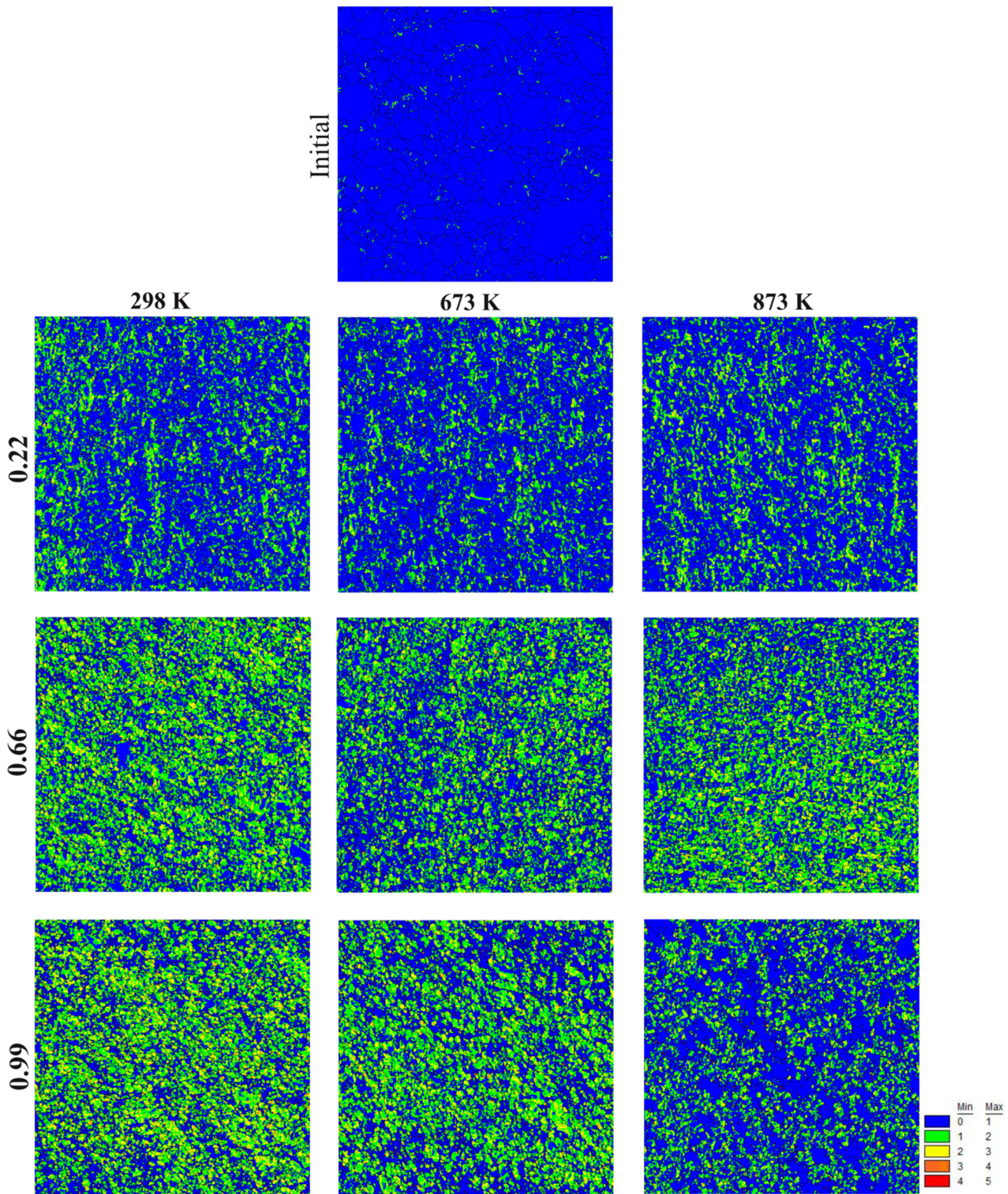


Fig. 8—Kernel average misorientation (KAM) maps as a function of shear strain after deformation at different temperatures.

leads to the fragmentation of the grains at larger strains. Figure 15(a) shows the schematic representation of the shearing process as suggested by Seshacharyulu *et al.*^[38]

A similar mechanism may be found by the previous researchers on shear deformation.^[7,9] Figure 15(b) shows an enlarged portion of the IPF map of the

sample deformed at a shear strain of 0.22 (Figure 3(a)). Figure 15(b) clearly captures the deformation mechanism presented in Figure 15(a). The KAM maps, as

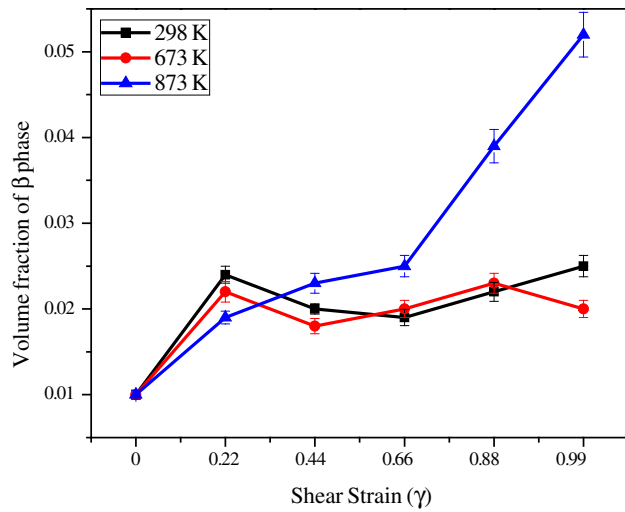


Fig. 9—Volume fraction of β grains as a function of shear strain after deformation at different temperatures.

presented in Figure 8, also shows that the localized deformation in the samples was observed to be homogeneous, which further supports the mechanism presented in Figure 15(a). With an increase in shear deformation, the amount of localized deformation was found to be increased at temperatures of 298 K and 673 K. However, this got decreased during deformation at 873 K because of the dynamic recrystallization. It can also be observed from Figure 7 that the VLAGBs increased progressively as a function of shear strain, which further supports the mechanism presented in Figure 15(a).

The occurrence of significant flow softening was observed at a temperature of 873 K (Figure 13). As suggested by many researchers,^[27,39,40] flow softening can be associated with dynamic restoration mechanisms like dynamic recovery/recrystallization processes, along with the increment in beta phase fraction by dynamic phase transformation. The minimum inflection point 'Q' in $\theta^* = -(\partial\theta/\partial\tau)$ vs shear stress (τ) curve (Figure 14(c)), which is an indication of the onset of DRX phenomenon,^[37] shows that the onset point of DRX was found to be approximately around 0.66 shear strain at 873 K. It was also observed in Figure 6(c) that a significant increment in DRX percentage after 0.66

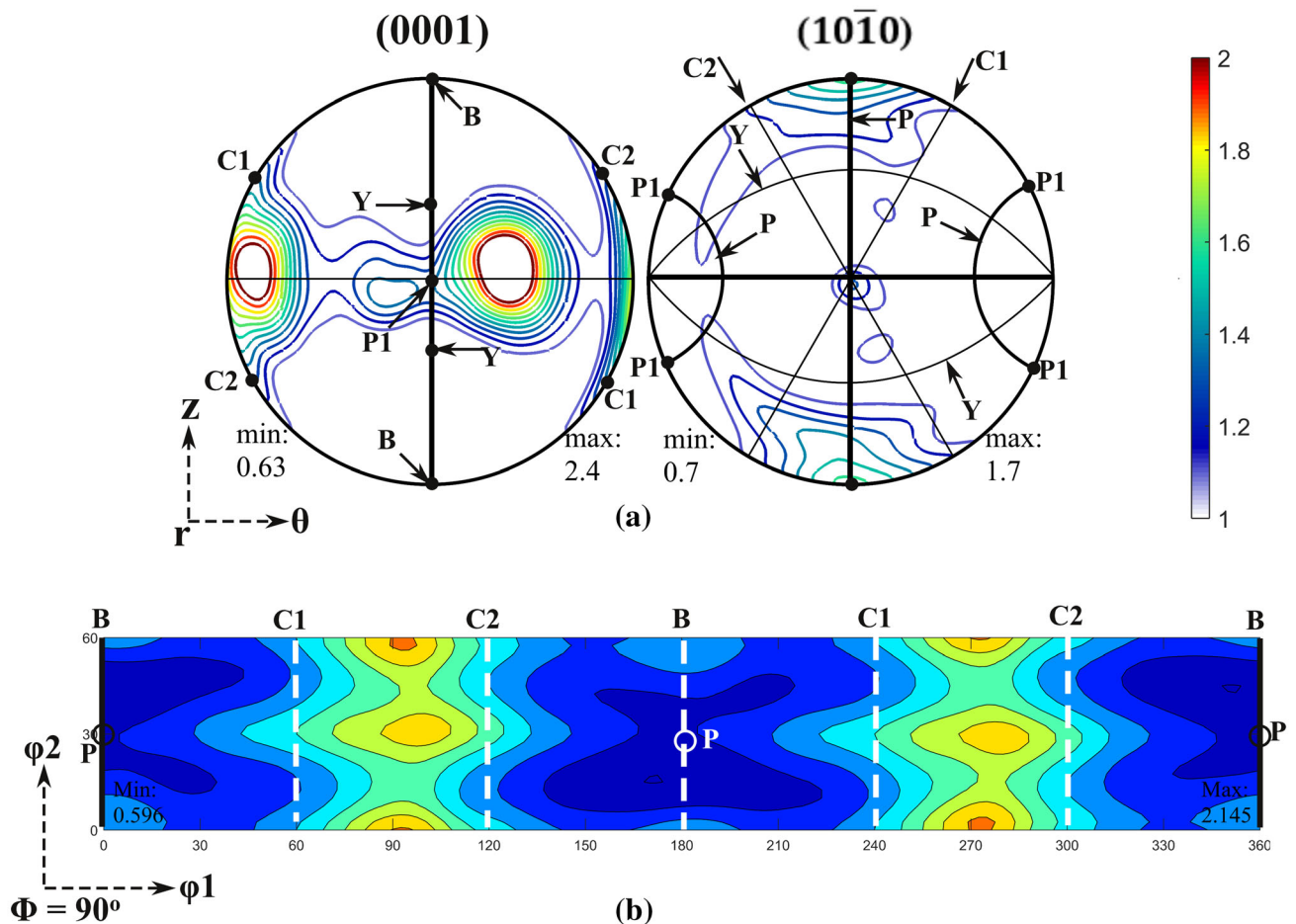


Fig. 10—Texture of the as-received Ti64 sample before subjected to torsion tests: (a) (0001) and $(10\bar{1}0)$ pole figures; (b) ODF at constant $\Phi = 90$ deg section. As reported in the literature,^[24] the ideal shear orientations observed in HCP metals/alloys are incorporated in (a, b).

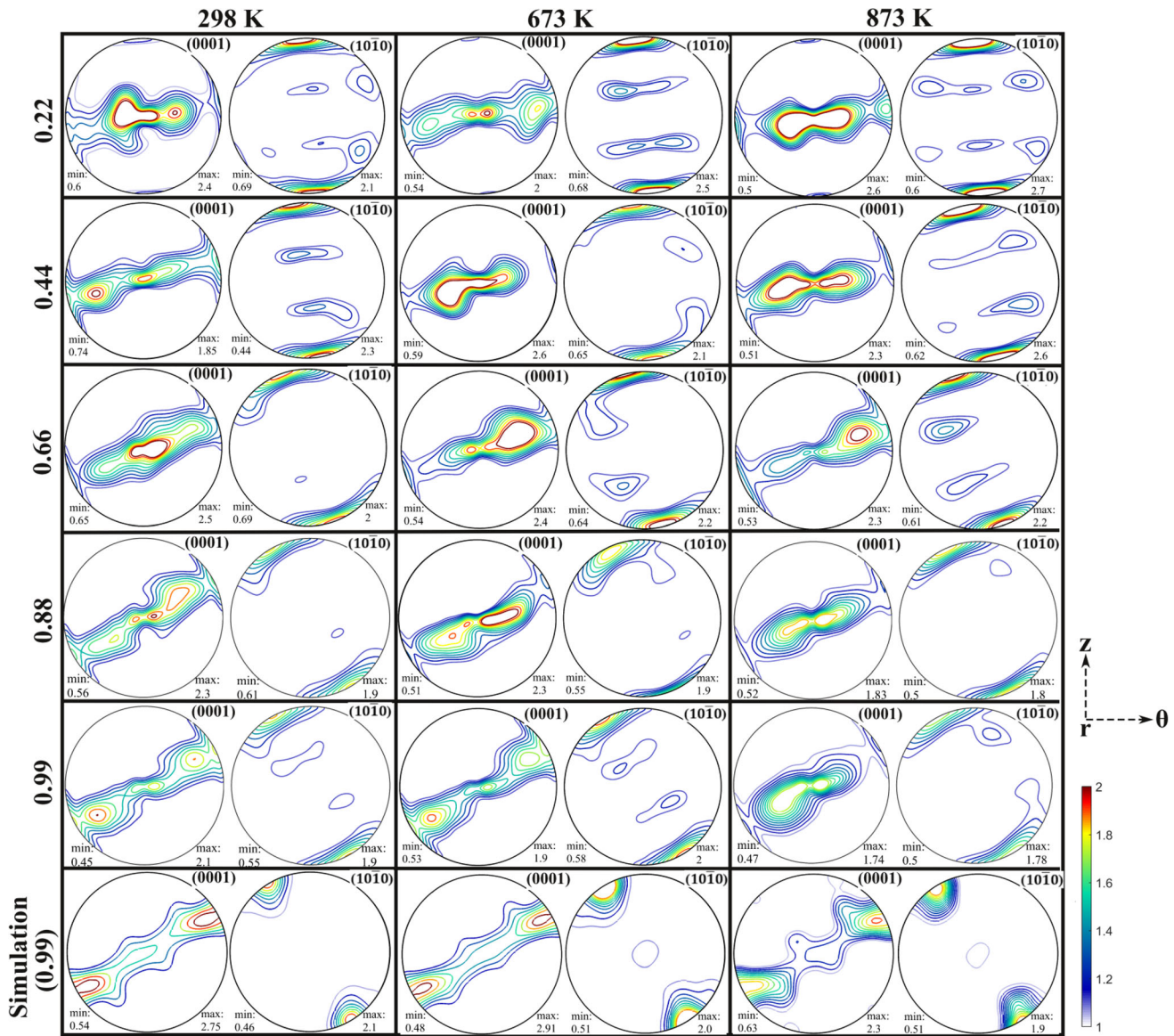


Fig. 11—(0001) and (10 $\bar{1}$ 0) pole figures of the samples as a function of shear strain after deformation at different temperatures. The simulated pole figures (through VPSC simulation) of the samples after deformation for a shear strain = 0.99 are also incorporated in the figure.

shear strain at 873 K. The gradual transformation of VLGB to LAGB and then to HAGB was the possible mechanism during DRX, as suggested by Sabat *et al.*^[35] and Lin *et al.*^[41] This mechanism can be attributed to the increment in HAGBs accompanied by a simultaneous reduction in VLGBs as observed in Figure 7(c).

Quantitative measurement of the volume fraction of β phase is shown in Figure 9. After the initial increment, the volume fraction of β phase was almost constant during deformation at temperatures of 298 K and 673 K. However, a significant increment in the volume fraction of β phase was observed at 873 K for shear strains > 0.66. It can be related to the deformation

induced phase transformation of $\alpha \rightarrow \beta$, normally observed along with the effect of flow softening.^[27,42–45] The stress gradient across the grain boundaries during hot deformation provides the driving force for the diffusion of α -stabilizer (Al) and β -stabilizer (V or Mo) which induces $\alpha \rightarrow \beta$ phase transformation.^[46] To discuss the β phase evolution, small portions of the IPF maps from Figure 5 are magnified and shown in Figure 16. The lattice rotation between adjacent β grains and the formation of LAGBs inside the β grain was noticed, which indicates the easier dislocation slip transfer across α/β grain boundaries.^[47] The α titanium transforms to β titanium by following the Burgers

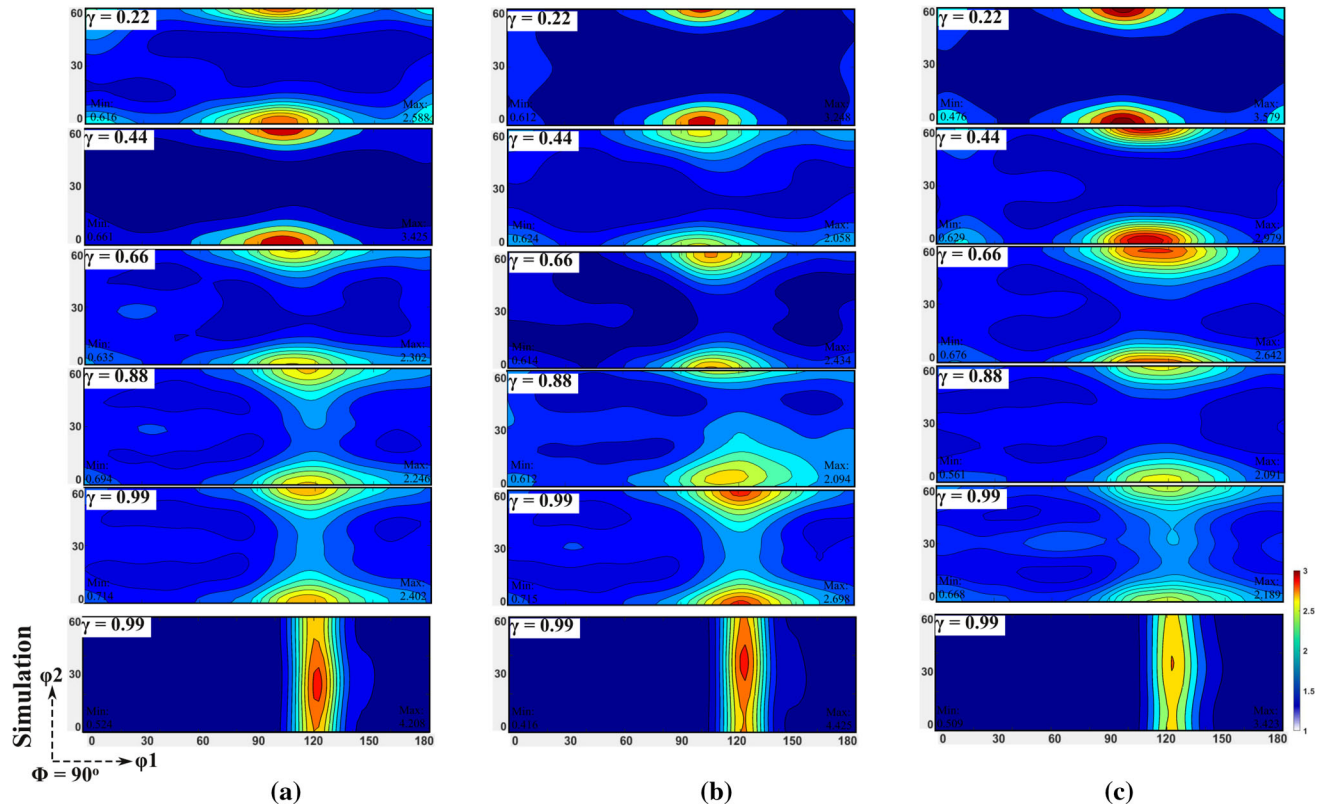


Fig. 12—ODFs at constant $\Phi = 90$ deg of the samples as a function of shear strain after deformation at different temperatures. The simulated pole figures (through VPSC simulation) of the samples after deformation for a shear strain = 0.99 are also incorporated in the figure.

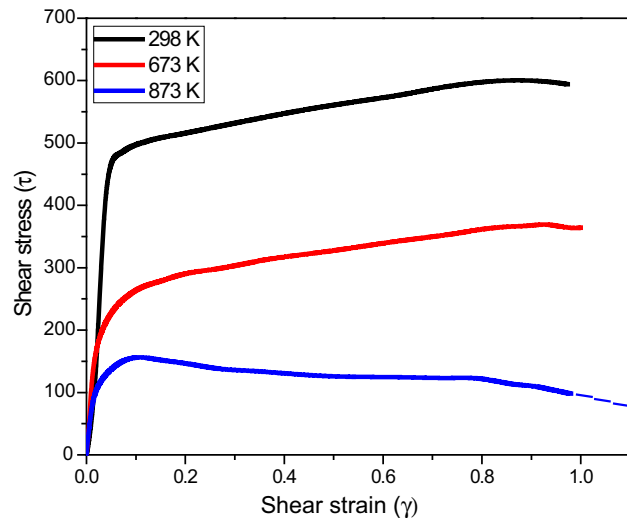


Fig. 13—Shear stress vs. shear strain curves of the samples during deformation at various temperatures.

orientation relationship (BOR), *i.e.*, $(0001)_\alpha // (110)_\beta$ and $[11\bar{2}0]_\alpha // [111]_\beta$.^[48,49] The BOR between α and β grains is shown by (0001) , $(11\bar{2}0)$, (110) , and (111) pole figures in Figure 16. The co-linearity of BOR was observed between α and β phase grains, which can be related to the ease of occurrence of dynamic transformation as suggested by Ji *et al.*^[47]

B. Texture Evolution

The initial texture of the as-received sample was formed at 90 deg from the ideal B fiber orientation, which is an extrusion type texture where the c -axis of the grains lies in the shear plane and perpendicular to the axial direction.^[19] During torsion deformation, the c -axis of grains rotated toward the axial direction or torsion axis which basically rotated the initial texture toward the ideal B fiber location in an anticlockwise direction as shown in Figure 11.^[25,26] It was further observed that the applied shear strain of 0.99 was not enough to reach the ideal B fiber location and it stopped at the ideal C2 fiber location (Figure 11). This was also evident in Figure 12, which represents the ODFs of the samples after shear deformation for different strain levels. The VPSC-simulated textures in the form of pole figures and ODFs were measured, and the results for a shear strain of 0.99 at all temperatures of deformation have been incorporated in Figures 11 and 12. A good match between the simulated and experimental textures at 298 K and 673 K was observed. However, a slight variation in the simulated texture was observed at 873 K, which might be related to the non-consideration of DRX and β I phase transition in the simulation. The texture evolution can be correlated with microstructural changes that occur during shear deformation. It has been reported that the split in the main texture fiber component can be related to the changes in grain shape during shear deformation.^[21,50] In the present study, the

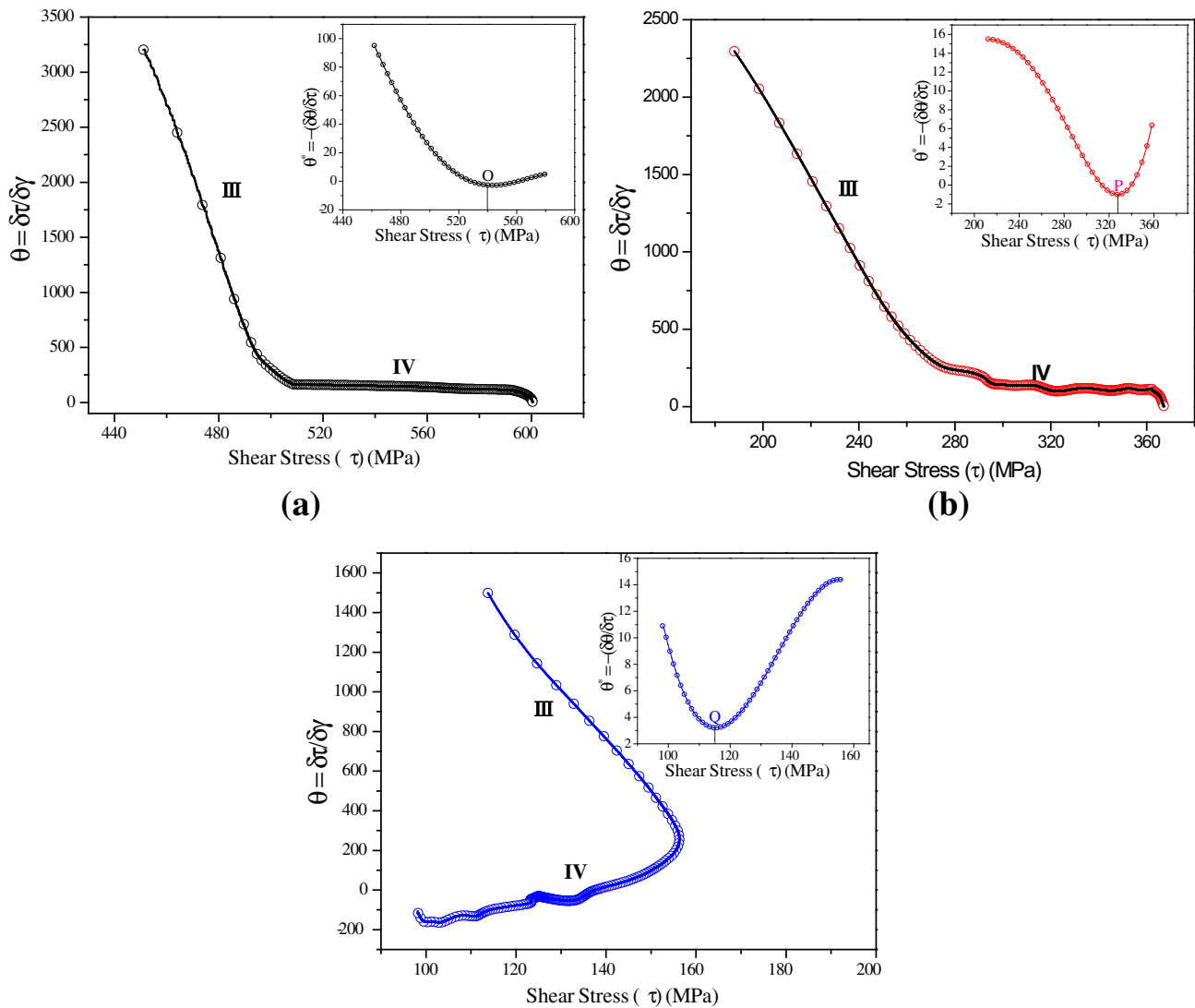


Fig. 14—First and second derivatives, i.e., θ and θ^* , of the shear stress vs. shear strain curve against shear stress: (a) 298 K; (b) 673 K; (c) 873 K.

undeformed texture transformed to partial fiber texture after shear deformation, which can be related to the change in microstructure from a wider grain size distribution to a near-equiaxed homogeneous microstructure. Similarly, the significant rotation and elongation of grains at higher shear strains changes the texture movement along φ_2 and φ_1 axes (Figure 12).

The slip activities as a function of shear strain during deformation at different temperatures are shown in Figure 17. Basal slip was found to be the dominant deformation mode, followed by prismatic and both pyramidal $\langle c+a \rangle$ I and II slip systems, all of which contribute to the shear deformation during torsion. A negligible contribution from the pyramidal $\langle a \rangle$ slip system was observed. The dominance of basal slip was also in correlation with the findings of Suwas *et al.*^[51] and Yapici *et al.*^[52] who examined the texture evolution of pure titanium and other hcp materials including Ti64

alloy, during the Equal Channel Angular Extrusion (ECAE) process which is also related to shear deformation. Although basal slip has higher activity than other slip systems, prismatic slip also contributed significantly to reproduce the experimental textures. It was observed that both basal and prismatic slip systems are opposing each other as their activities got changed reversely during deformation (Figure 17). After a shear strain of 0.66, both basal and prismatic slip activities were maintained constant at 298 K and 673 K. So to compensate the larger shear deformation, the activity of pyramidal $\langle c+a \rangle$ slip system was gradually increased with increasing the shear strain. However, the basal slip activity was noticed to increase with strain at deformation temperature of 873 K. This is in consistent with the works of Li *et al.*^[53] who found the domination of basal slip at higher temperatures of deformation, which they relate to the increment in Al

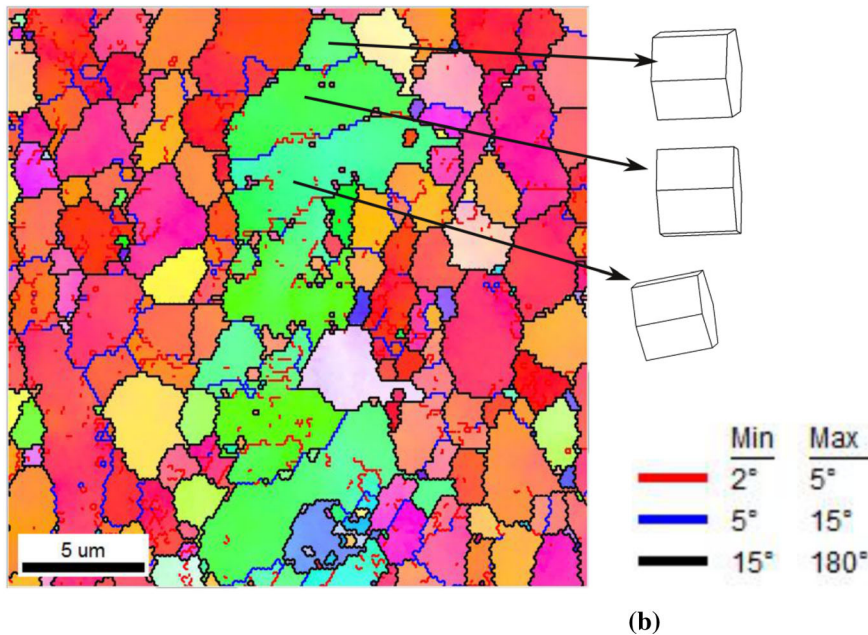
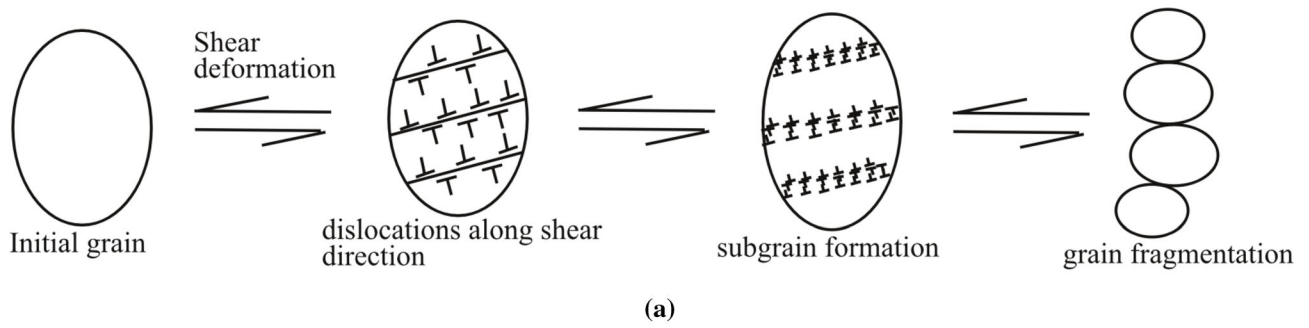


Fig. 15—(a) A schematic representation of possible mechanism of grain fragmentation during shear deformation; (b) IPF map of the sample after deformation for a shear strain of 0.22 at 298 K. In (b) different grain boundaries are incorporated to capture the fragmentation of a grain during deformation.

content. The movement of texture components along φ_1 or Φ can be related to the activity of $\langle a \rangle$ type basal, prismatic, and pyramidal $\langle c+a \rangle$ slip systems as reported by Sabat *et al.*^[35] The rotation of the partial fiber texture along φ_1 correlates to the activity of basal and prismatic slip, and the activity of pyramidal $\langle c+a \rangle$ slip system beyond a shear strain of 0.66 moves the texture component along φ_2 axis.

VI. CONCLUSIONS

The following conclusions can be drawn from the present study:

1. The initial microstructure consisting of a large volume fraction of both fine and coarse grains got transformed into a near-equiaxed homogeneous microstructure during shear deformation at all temperatures. Grain fragmentation by subgrain formation was observed to be the possible mechanism for obtaining microstructural homogeneity.
2. DRX was observed in the samples during deformation at higher temperatures. However, this was significant at 873 K for shear strains > 0.66 . The DRX mechanism can be attributed to the increment in HAGBs accompanied by a simultaneous reduction in VLAGBs.
3. The occurrence of dynamic transformation of $\alpha \rightarrow \beta$ was also observed at a deformation temperature of 873 K, and this can be correlated to the BOR between α and β grains.
4. The flow stress values decreased as the temperature of deformation increased. Further, deformation at a temperature of 873 K showed significant flow softening which can be attributed to the dynamic

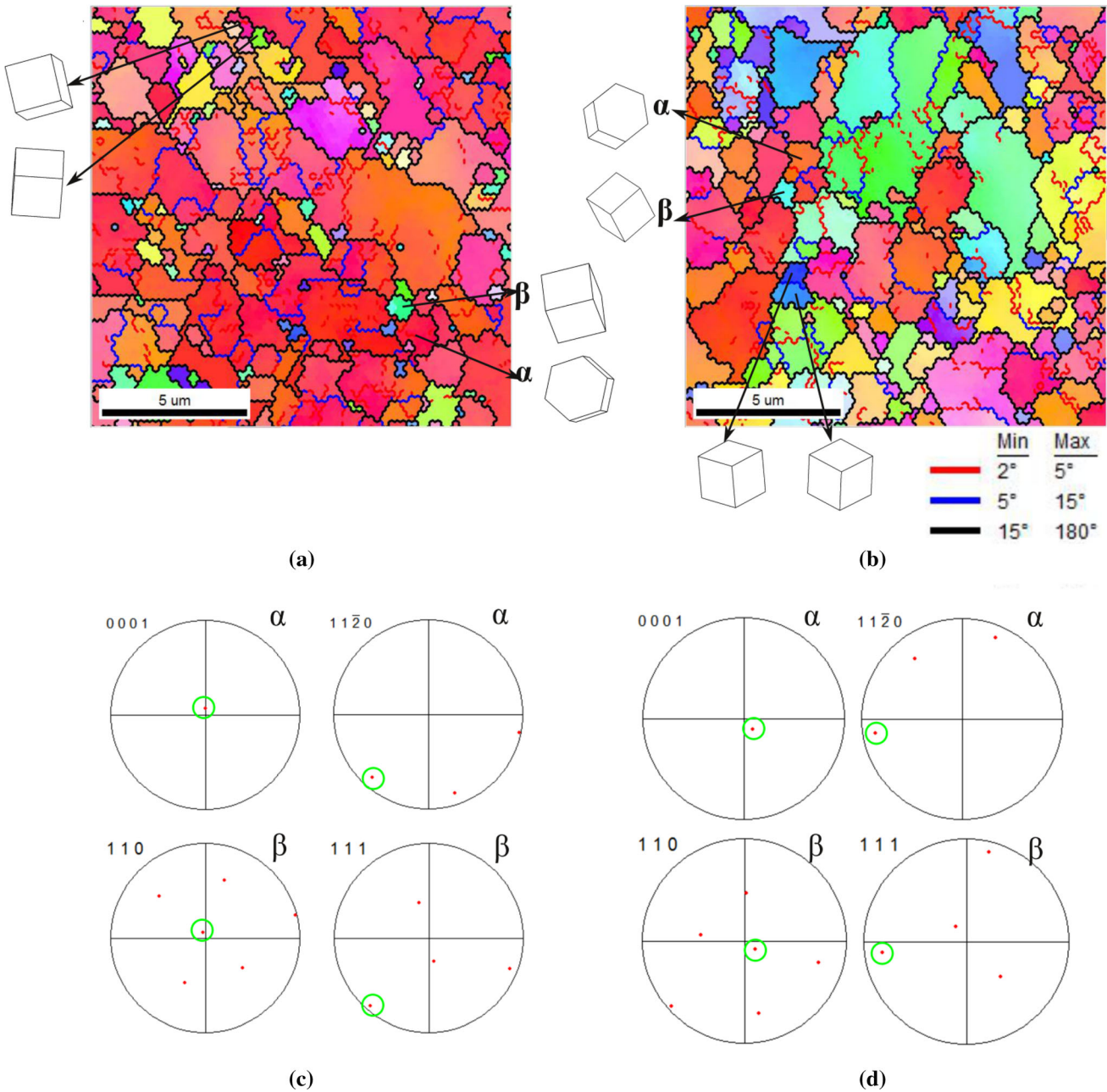


Fig. 16—(a, b) Magnified view of marked regions [in Fig. 5(d, e)] superimposed with different grain boundaries, (c, d) Pole figures of α and β grains marked in (a, b).

recrystallization and increment in β volume fraction. Higher strain hardening rate was observed during room temperature deformation as compared to those at high temperatures. Hardening curves got shifted to lower stress values with increase in the temperature of deformation.

5. Bulk texture measurements showed that initial fiber texture got rotated up to 30 deg along the shear

direction and reached up to the ideal C2 fiber orientation after deformation. VPSC simulation predicted that the dominant deformation modes during shear deformation of Ti64 were basal slip followed by prismatic, pyramidal $\langle c+a \rangle$ I and II slips. Pyramidal $\langle a \rangle$ slip had negligible effect during the shear deformation.

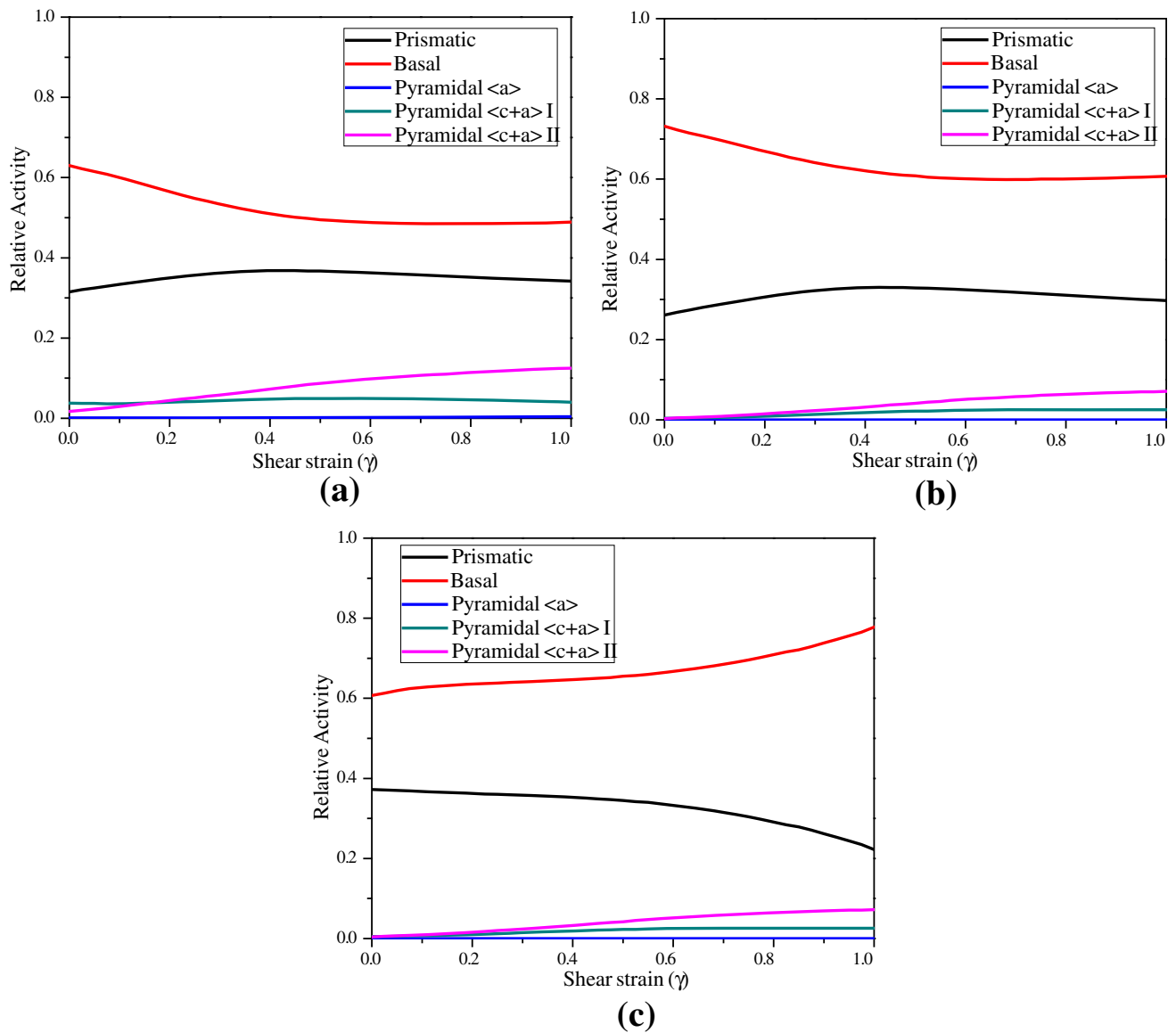


Fig. 17—Relative activities of various slip systems for the samples during deformation at various temperatures of: (a) 298 K; (b) 673 K; (c) 873 K.

ACKNOWLEDGMENTS

The authors thank Prof. S. Suwas, Dept. of Materials Engg., IISc Bangalore, for conducting torsion tests of the samples in his laboratory. The authors also thank Prof. I. Samajdar for conducting EBSD measurements of the samples in his laboratory, National Facility on OIM and Texture, at Dept. of Metallurgical Engg. and Materials Science, IIT Bombay, Powai, Mumbai. The authors acknowledge the DST-FIST-supported XRD-Texture laboratory at Dept. of Metallurgical & Materials Engg., NIT Rourkela, for bulk texture measurements of the samples.

CONFLICT OF INTEREST

On behalf of all authors, the corresponding author states that there is no conflict of interest.

REFERENCES

1. R.R. Boyer: *Mater. Sci. Eng. A*, 1996, vol. 213, pp. 103–14.
2. I. Inagaki, Report No. 106, Nippon Steel & Sumitomo Metal, Osaka city, Technical Report, July 2014.
3. C. Leyens and M. Peters: *Titanium and Titanium Alloys: Fundamentals and Applications*, Wiley-VCH, Weinheim, 2003.
4. B.D. Bishoyi, R.K. Sabat, J. Sahu, and S.K. Sahoo: *Mater. Sci. Eng. A*, 2017, vol. 703, pp. 399–12.

5. Y. Fan, W. Tian, Y. Guo, Z. Sun, and J. Xu: *Adv. Mater. Sci. Eng.*, 2016, vol. 2016, pp. 1–10.
6. S.V. Zherebtsov, E.A. Kudryavtsev, G.A. Salishchev, B.B. Straumal, and S.L. Semiatin: *Acta Mater.*, 2016, vol. 121, pp. 152–63.
7. J. Zhang, H. Li, and M. Zhan: *Manuf. Rev.*, 2020, vol. 7, pp. 1–14.
8. I. Weiss, F.H. Froes, D. Eylon, and G.E. Welsch: *Metall. Trans. A*, 1986, vol. 17, pp. 1935–47.
9. T. Seshacharyulu, S.C. Medeiros, W.G. Frazier, and Y.V.R.K. Prasad: *Mater. Sci. Eng. A*, 2002, vol. 325, pp. 112–25.
10. J. Gil Sevillano, P. Van Houtte, and E. Aernoudt: *Prog. Mater. Sci.*, 1981, vol. 25, pp. 69–134.
11. S.C. Shrivastava, J.J. Jonas, and G. Canova: *J. Mech. Phys. Solids*, 1982, vol. 30, pp. 75–90.
12. F. Montheillet, M. Cohen, and J.J. Jonas: *Acta Metall.*, 1984, vol. 32, pp. 2077–89.
13. T. Pettersen and E. Nes: *Metall. Mater. Trans. A*, 2003, vol. 34A, pp. 2727–36.
14. E. Cakmak, H. Choo, K. An, and Y. Ren: *Acta Mater.*, 2012, vol. 60, pp. 6703–13.
15. L.S. Tóth, J.J. Jonas, D. Daniel, and J.A. Bailey: *Textures Microstruct.*, 1992, vol. 19, pp. 245–62.
16. P. Sanchez, A. Pochettino, T. Chauveau, and B. Bacroix: *J. Nucl. Mater.*, 2001, vol. 298, pp. 329–39.
17. S. Biswas, B. Beausir, L.S. Toth, and S. Suwas: *Acta Mater.*, 2013, vol. 61, pp. 5263–77.
18. H. Xiao, Z. Yang, J. Li, and Y. Wan: *Materials.*, 2021, vol. 14, p. 2067.
19. H. Chen, B. Song, N. Guo, T. Liu, T. Zhou, and J. He: *Met. Mater. Int.*, 2019, vol. 25, pp. 147–58.
20. X.Q. Guo, W. Wu, P.D. Wu, H. Qiao, K. An, and P.K. Liaw: *Scr. Mater.*, 2013, vol. 69, pp. 319–22.
21. B. Beausir, L.S. Tóth, F. Qods, and K.W. Neal: *J. Eng. Mater. Technol.*, 2009, vol. 131, pp. 0111081–01110815.
22. N.P. Gurao and S. Suwas: *Mater. Sci. Forum.*, 2012, vol. 702, pp. 826–9.
23. S. Balasubramanian and L. Anand: *Acta Mater.*, 2002, vol. 50, pp. 133–48.
24. ***.
25. H. Chen, F. Li, J. Liu, J. Li, X. Ma, and Q. Wan: *Metall. Mater. Trans. A*, 2017, vol. 48, pp. 2396–409.
26. B. Beausir, L.S. Tóth, and K.W. Neale: *Acta Mater.*, 2007, vol. 55, pp. 2695–705.
27. B. Guo, S.L. Semiatin, J.J. Jonas, and S. Yue: *J. Mater. Sci.*, 2018, vol. 53, pp. 9305–15.
28. B. Guo, C. Aranas, A. Foul, X. Ji, A. Fall, M. Jahazi, and J.J. Jonas: *Mater. Sci. Eng. A*, 2018, vol. 729, pp. 119–24.
29. C.N. Tome and R.A. Lebensohn: *VPSC Manual for Code Version 7c*, National Laboratory L.A., 2010.
30. S. Zaefferer: *Mater. Sci. Eng. A*, 2003, vol. 344, pp. 20–30.
31. G.R. Canova, U.F. Kocks, and J.J. Jonas: *Acta Metall.*, 1984, vol. 32, pp. 211–26.
32. G. Lutjering and J. Williams: *in: Titanium*, 2nd ed. Springer, New York, 2007.
33. J. Galan-Lopez, S. Naghdy, P. Verleysen, L. Kestens, F. Coghe, L. Rabet, and J. Degrieck: *IOP Conf. Ser.: Mater. Sci. Eng.*, 2015, vol. 82, pp. 233–345.
34. M. Paghandedeh, A. Zarei-Hanzaki, H.R. Abedi, Y. Vahidshad, J. Kawalko, D. Dietrich, and T. Lampke: *J. Mater. Res. Technol.*, 2021, vol. 10, pp. 1291–300.
35. R. K. Sabat, M.V.S.S.D.S.S. Pavan, D. S. Aakash, M. Kumar, and S. K. Sahoo: *Philos. Mag.*, 2018, vol. 98, pp. 2562–2581.
36. A. Nadai: *Theory of Flow and Fracture*, McGraw-Hill, New York, 1950.
37. E.I. Poliak and J.J. Jonas: *Acta Mater.*, 1996, vol. 44, pp. 127–36.
38. T. Seshacharyulu, S.C. Medeiros, J.T. Morgan, J.C. Malas, W.G. Frazier, and Y.V.R.K. Prasad: *Scr. Mater.*, 1999, vol. 41, pp. 283–8.
39. Y.V.R.K. Prasad and T. Seshacharyulu: *Int. Mater. Rev.*, 1998, vol. 43, pp. 243–58.
40. T. Furuhashi, B. Poorganji, H. Abe, and T. Maki: *JOM.*, 2007, vol. 59, pp. 64–7.
41. L. Jin, D. Lin, D. Mao, X. Zeng, B. Chen, and W. Ding: *Mater. Sci. Eng. A*, 2006, vol. 423, pp. 247–52.
42. T. Zhang, Y. Liu, D.G. Sanders, B. Liu, W. Zhang, and C. Zhou: *Mater. Sci. Eng. A*, 2014, vol. 608, pp. 265–72.
43. H.S. Yang, G. Gurewitz, and A.K. Mukherjee: *Mater. Trans. IIM*, 1991, vol. 32, pp. 465–72.
44. R. Ding, Z.X. Guo, and A. Wilson: *Mater. Sci. Eng. A*, 2002, vol. 327, pp. 233–45.
45. H. Matsumoto, K. Yoshida, S.H. Lee, Y. Ono, and A. Chiba: *Mater. Lett.*, 2013, vol. 98, pp. 209–12.
46. K. Wang, G. Liu, W. Tao, J. Zhao, and K. Huang: *Mater. Charact.*, 2017, vol. 126, pp. 57–63.
47. X. Ji, B. Guo, F. Jiang, H. Yu, D. Fu, J. Teng, H. Zhang, and J.J. Jonas: *J. Mater. Sci. Technol.*, 2020, vol. 36, pp. 160–6.
48. N. Stanford and P.S. Bate: *Acta Mater.*, 2004, vol. 52, pp. 5215–24.
49. D. Bhattacharyya, G.B. Viswanathan, R. Denkenberger, D. Furrer, and H.L. Fraser: *Acta Mater.*, 2003, vol. 51, pp. 4679–91.
50. I.J. Beyerlein, R.A. Lebensohn, and C.N. Tome: *Mater. Sci. Eng. A*, 2003, vol. 345, pp. 122–38.
51. G.G. Yapici and I. Karaman: *Mater. Sci. Eng. A*, 2009, vol. 503, pp. 78–81.
52. S. Suwas, B. Beausir, L.S. Tóth, J.J. Fundenberger: *Acta Mater.* 2011, 59:1121–1133.
53. H. Li: *Analysis of the deformation behavior of the hexagonal close packed alpha phase in titanium and titanium alloys*, Doctoral dissertation, Michigan State University, United States, 2013.

Publisher's Note Springer Nature remains neutral with regard to jurisdictional claims in published maps and institutional affiliations.